Coupling of magnetoresistance switching and glassy magnetic state at the metal-insulator transition in Ruddlesden-Popper manganate $Ca_4Mn_3O_{10}$

Manimuthu Periyasamy, Øystein S. Fjellvåg, Helmer Fjellvåg and Anja O. Sjåstad*

Centre for Materials Science and Nanotechnology, Department of Chemistry, University of Oslo, PO Box 1033, N-0315 Oslo Norway
E-mail: a.o.sjastad@kjemi.uio.no, helmer.fjellvag@kjemi.uio.no and magnetmanidnp@gmail.com

Abstract

Electronic phase separation is a frequent ingredient of the physics of manganites for which the colossal magnetoresistance (CMR) phenomenon is at debate. We investigate the switchable magnetoresistance (MR) effect of the Ruddelsden-Popper (RP) oxide $Ca_4Mn_3O_{10}$ (CMO), which shows a metal-to-insulator transition (MIT) at 70 K (T_{MIT}). The static (DC) and dynamic (AC) magnetic susceptibilities of CMO indicate an unusual magnetic phase coexistence below the Néel temperature (T_N) i.e., at T_{MIT}, which we describe as a glassy magnetic behavior. Furthermore, by means of synchrotron X-ray diffraction, we observed a structural anomaly directly associated with the MIT. Hence, the onset of glassiness correlates with a slight structural distortion. Interestingly, CMO displays a large positive magneto-resistance (PMR) effect (up to 550 % at 4 K) in the metallic state below T_{MIT}, while a small negative magneto-resistance (NMR) effect (-3.5 % at 112 K) in the insulating region above T_{MIT}. At T_{MIT}, the PMR switches to NMR behavior. PMR is probably induced via enhancing the exchange interaction by localization of itinerant moment resulting in formation of magnetic polarons, whereas NMR is possibly due to reduced electron-spin scattering. This appears to be a special type of magnetoresistance, different from regular observations, and may open a new avenue in searching for exotic phenomena in manganese-based CMR materials.

Introduction

Mixed valence perovskite-type manganites have intensively been studied since the discovery of colossal magnetoresistance (CMR), with potential applications as magnetic field sensors and memory devices in mind [1-4]. The underlying mechanism for CMR receives significant attention. Efforts in theory and experiment reveal that mechanisms connected with double exchange, Jahn–Teller distortions and Anderson type localization are insufficient for convincingly explain CMR phenomena [5, 6]. The detailed studies by Dagotto *et al.* [7] showed that manganites, being strongly correlated electron systems, exhibit a particular intrinsic tendency towards inhomogeneous states that may involve paramagnetic, antiferromagnetic (AFM), metallic ferromagnet (FM), insulating FM and insulating charge-ordered (CO) phases.

The CMR behavior depends on a delicate interplay of charge, spin, orbital and lattice degrees of freedom. Experimental studies on manganites have confirmed the occurrence of inhomogeneous states and the presence of competing states/phases [8, 9]. The CMR phenomenon is linked to phase coexistence and competition between different magnetic and electrical states. However, the structure dimensionality also plays an essential role in the nature of the interactions, and the CMR effect is larger in layered manganites [10, 11].

The Ruddelsden-Popper (RP) phases, $A_{n+1}B_nO_{3n+1}$ (n = 1, 2, 3) have a layered like structure where the perovskite-type blocks (n) are separated by rock salt like layers. RP phases provide, in this sense, an invaluable experimental system for studying effects of dimensionality [12]. The existence of (half) a rock-salt layer (AO) between the perovskite-type blocks ($A_nB_nO_{3n}$) increases the interlayer separation between slabs with perovskite type atomic arrangement, thereby affecting exchange interactions in the stacking direction. This causes an anisotropic reduction in the 3*d* bandwidth and modifies the magnetic and electric properties of RP phases [13].

Among the n = 3 RP phases (RP3), $Ca_4Mn_3O_{10}$ (CMO) attracts particular interest as it shows features of coexistence of AFM and weak ferromagnetic (WFM) well below T_N = 115 K [14-16]. In addition, CMO was found to undergo a metal-insulator-transition (MIT) below T_N [17]. Moreover, CMO displays magnetoresistance (MR) ratios up to 40 % [18]. The situation with competing electronic phases (AFM+WFM) that promotes the MR property and the MIT nature of CMO is not well understood. To our knowledge, there is very scarce data on the MR property and MIT of CMO. To clarify the exotic physical properties of CMO and its interrelations, detailed studies of the structural, magnetic and transport properties are required. Herein we report for the first-time detailed DC- and AC- susceptibility studies along with measurements of electric properties. Importantly, the changes in electronic properties are complemented by temperature-dependent synchrotron powder X-ray diffraction (XRD) data, which provide novel insight concerning correlated structural anomalies. We also show for the first time that CMO exhibits a magnetic phase coexistence below the Néel transition, which, crucially in the search for new colossal magnetoresistance materials, drives the MIT.

Experimental

Phase-pure polycrystalline $Ca_4Mn_3O_{10}$ was synthesized according to the citric acid method [19, 20]. The starting materials were: calcium nitrate, $Ca(NO_3)_2 \cdot xH_2O$ (99.97 %, Sigma Aldrich); manganese nitrate, $Mn(NO_3)_2 \cdot 4H_2O$ (98.5 %, Merck) and citric acid monohydrate, $C_3H_4(OH)(COOH)_3 \cdot H_2O$ (98 %, Sigma Aldrich). All chemicals were used as received. Stoichiometric amounts of calcium nitrate and manganese nitrate salts were precisely weighted and dissolved in deionized water with stirring. After complete dissolution, the solution was heated while stirring until boiling. At this stage, citric acid monohydrate was added during stirring and heating. The solution was left boiling until the formation of a gel, and thereafter dehydrated in a heating cabinet at 453 K overnight. Subsequently, calcination was done in alumina crucibles at 673 K for 4 h and 1073 K for 1 h in static air, in order to remove the organic matter and to decompose the nitrate mixture. The resulting powders were ground, pelletized,

and sintered at 1573 K in air for one week to produce a pure CMO phase. The sintering temperature is below the melting point of the compound (~1623 K [15]).

Low-temperature synchrotron powder XRD data were measured at BM01 (Swiss-Norwegian Beamlines, SNBL) at ESRF in Grenoble, France, at a wavelength of $\lambda = 0.71490$ Å and using a 2D PILATUS2M detector [21]. The finely crushed powder was filled in a 0.1 mm diameter borosilicate capillary and powder diffraction patterns were collected at 8, 10, 20, 40, 60, 70, 80, 90, 100, 120, 140 and 180 K, using a He cryostat. The 2D-images were integrated using the SNBL Bubble software to provide 1D diffraction patterns from $0 < 2\theta < 34.8°$ with a step size of 0.01°. Diffraction patterns were collected at several detector distances (100 – 500 mm) in order to cover a large Q-range and achieve optimal angular resolution. The multiple patterns collected at a given temperature were refined simultaneously within the same crystal structure model using the TOPAS V5 software [22]. Tables S1 and S2 show how different parameters were simultaneously refined for several diffraction patters with the aim to reduce the uncertainties. Crystallographic information is given in Tables S3 - S7. Electric resistivity, magnetic- and MR properties were measured using a Quantum Design Physical Property Measurement System (PPMS). Electric resistivity data were measured on a bar-shaped sintered sample, using in-line four-point contact geometry and a DC current of 1 mA at temperatures between 4 and 300 K. The magnetic measurements were done in both static (DC) and dynamic (AC) modes as a function of temperature and for applied magnetic fields up to 9 T. DC magnetic measurements were performed in zero-field-cooling (ZFC) and field-cooling (FC) conditions to understand the nature of magnetic interactions in the temperature range 4 - 300 K. The real (χ') and imaginary (χ'') components of the AC (linear and non-linear) magnetic susceptibility and its higher orders (second and third harmonics) were measured (with and without filed) as a function of temperature in the range 4 – 170 K at an AC drive amplitude h = 5 Oe with different frequencies up to 9917 Hz to find out the glassy magnetic transition. Field dependent MR measurements were carried out at 4, 50, 65, 75, 100 and 112 K.

Results and Discussion

The resistivity data in Fig. 1 reveals a transition at 70 K from a high-temperature insulating state to a low-temperature metallic state, where the resistivity changes by several orders of magnitude. We describe this transition as an MIT. Similar behavior for CMO has been reported by Rossel *et al.* [17]. Although various mechanisms have been proposed, the MIT remains among the least understood phenomena in condensed matter systems [23]. However, its occurrence appears always to be accompanied by structural effects [24], but the involved changes can be minimal. Therefore, we have carefully explored whether a structural transition can be associated with the observed MIT in CMO. Up to now, no such data have been available.

Synchrotron XRD measurements were carried out at selected temperatures with a focus on the temperature range below and around the MIT (Fig. 2). The sample was initially cooled to 8 K before subsequent stepwise heating. At 8 K, CMO takes the same orthorhombic RP3 structure (space group *Pbca*) as at room temperature, see Fig. 3 and Table S3. No impurities

are observed in the sample. The structural changes are minor upon heating, and cannot be observed by visual inspection of the diffraction patterns. However, from Rietveld refinements, we are able to extract detailed structural information and we find pronounced changes at an atomic scale. Crystal structure information was obtained at 12 different temperatures between 8 and 180 K by means of Rietveld refinements, exemplified by unit cell parameters and coordinates listed in SI, Table S4 - S7. In general, we observe an increase in unit cell dimensions on heating. However, at 70 K a quite abrupt contraction in all dimensions is observed (Fig. 4), coinciding with the MIT temperature (T_{MIT}), an indication of strong coupling between charge transport and crystal lattice. No change of symmetry occurs along with the structural anomaly. To the best of our knowledge, this is the first direct observation of a structural change associated with the MIT for CMO. We further note that no change in unit cell parameters is observed at T_N.

The Rietveld refinements provide data on atomic coordinates and hence changes in bonds and angles at the MIT. However, the structural complexity of the RP3 phase, along with more heavily scattering calcium and manganese atoms, implies uncertainties in the oxygen coordinates and the corresponding bond lengths and angles. Nevertheless, the analysis reveals changes in atomic coordinates in the range of the MIT and the unit cell contraction at 70 K, which in turn affects the bond lengths, Fig. 5. Our analysis shows that the Mn1 octahedra are less distorted than the Mn2 octahedra, *i.e.* the variation in bond lengths is larger. Further, the Mn1 octahedra are more distorted below the MIT, while the Mn2 octahedra are less distorted, meaning that the two Mn coordination's becomes somewhat more similar at low temperatures Below the MIT, the Mn2 moves away from the O3 and closer to the center of the octahedron. Additionally, the O1 (oxygen atom between Mn1 and Mn2) drives towards the central perovskite layer (Mn1). Hence, there are atomic rearrangements in CMO that relates to the MIT. The changes are small, yet significant. Based on these results, we are confident that the MIT is coupled to structural changes. A detailed analysis of CMO by neutron diffraction is at hand (see Ref.15), however, additional information as function of temperature is highly desirable and is left for future work.

To further reveal the MIT nature, more detailed studies were carried out regarding the magnetic properties. In general, MITs are typically accompanied by a magnetic transition [11, 25]. Hence, we performed AC and DC magnetic susceptibility measurements as a function of temperature and applied magnetic field. Figure 6a shows the temperature dependence of the DC magnetic susceptibility, $\chi_{dc}(T)$, in field cooled (FC)/zero-field-cooled (ZFC) conditions measured in 0.1 T. Strong irreversibility in FC and ZFC susceptibilities indicates a large magnetic anisotropy in the system and is in qualitative agreement with previous results [15, 16]. The ZFC curve shows a peak at 115 K, pointing towards typical AFM behavior (Néel temperature, T_N). This shows that long range magnetic order is present well above the MIT temperature and indicates no coupling between these two phenomena. One of the notable features of Figure 6a is that the FC data show two clear upturns at low temperatures ($T < T_N$), different from the peak-shaped nature of the AFM transition seen in ZFC. Noteworthy, the first observed upturn in $\chi_{dc}(T)$ peaks at around 70 K, then decreases, and again peaks at $T < 15$ K. This suggests a more complex magnetic behavior and is not seen in the ZFC data.

To probe the complex magnetic character (below the AFM transition) in detail, the $\chi_{dc}(T)$ behavior was studied at various DC field strengths under FC conditions; see Fig. 6b for fields in the range of 50 Oe to 0.7 T. On increasing field strengths, a new magnetic feature appears at around 70 K i.e., at T_{MIT}. This magnetic anomaly correlates with the orthorhombic structural distortion that occurs in the same temperature interval (Fig. 4 and 5).

The magnetic structure of each perovskite block in CMO is of G-type, with antiferromagnetic spin alignment between nearest Mn(IV) neighbors. As will be discussed below, there are indications for a weak spin canting. Hence, antisymmetric exchange interaction may exist together with symmetric super-exchange in the MIT temperature range. When the applied magnetic field is increased, the canting will increase, yielding more spins aligned parallel to the field. This results in (sudden) increase in magnetization. Therefore, a peak in χ_{dc} is observed which is increasing in magnitude with applied field strengths. We carefully checked that this unusual magnetic anomaly at 70 K did not corresponds to any potential magnetic impurity such as manganese oxides (Mn_3O_4 – FM at 40 K and others have AFM transitions at some 120 K), $CaMn_2O_4$ (AFM at 220 K), and $CaMnO_3$ (AFM at 125 K) and its reduced phases (Ca_2MnO_4 – AFM at 115 K, $Ca_3Mn_2O_7$ – AFM at 123 K). The upturn in FC-$\chi_{dc}(T)$ below ~15 K (observed in all external applied DC fields) is likely due to residual paramagnetic spins, intrinsic in nature or from slight amounts of 3d-impurities. The presence of two magnetic transitions, at 115 and 70 K, could be a characteristic of a glassy magnetic state [26]. However, the possible presence of a glassy-like component in CMO remains open.

The AC susceptibility (linear and non-linear) technique is a powerful method to e.g. study glassy magnetic systems. Figure 7(a) and 7(b) reveals the real (χ') and imaginary part (χ'') part of the first harmonic of AC susceptibility (χ_{ac}) with zero external DC field. Both χ' and χ'' were measured as a function of temperature from 5 to 170 K with varying frequency (117, 1117 and 9917 Hz) at a fixed AC drive amplitude of 5 Oe. The results obtained for the temperature-dependent in-phase ac susceptibility, $\chi'(T)$ shows a peak at 115 K (Fig. 7a). The out-of-phase ac susceptibility, $\chi''(T)$ does not show any peak at the same temperature (Fig. 7b) which is in compliance with T_N [27]. We note that the magnitude of $\chi'(T)$ does not decay rapidly as the temperature is further decreased below T_N, which is consistent with a canted AFM ordering at low temperatures.

To understand the origin of the unusual magnetic behavior at 70 K (at T_{MIT}), χ_{ac}-FC was also studied at different DC field strengths. For 1 T DC field, the $\chi'(T)$ (Fig. 8a) shows an additional peak at around 70 K (consistent with χ_{dc}) and interestingly the $\chi''(T)$ appears to exhibit a weak peak at the corresponding temperature (Fig. 8b). This is attributed to a spontaneous magnetization contribution (ferromagnetism) in this temperature range [27, 28]. Nonlinear $\chi(T)$ measurements (second and third harmonics) were performed in a DC field of 1 T to elucidate the possible presence of ferromagnetism and its intrinsic nature [28]. The appearance of peaks [both in $\chi'(T)$ and $\chi''(T)$] in second harmonics (2 hr) (Fig. 9a) and a positive [$\chi'(T)$] and negative [$\chi''(T)$] crossover of third harmonics (3 hr) (Fig. 9b) at and below 70 K substantiates the claim of a spontaneous moment residing within the CMO [29, 30].

Isothermal *M-H* magnetization studies were carried out at 4, 25, 50, 100 and 150 K, Fig. 10. Saturation was not obtained within the applied field range. Figure 10 indicates an almost linear M(H) behavior at moderate fields, however, showing a weakly S-shaped slope at low fields. However, a notable coercivity and remanence is observed below T_N. Importantly, the *M-H* loop behavior at 50 K exhibits higher values of remanence and coercivity compared to the values at 4 and 25 K. Thus, the magnetic hysteresis loops measured below 70 K indicate that CMO is a canted antiferromagnet in which the canting of magnetic spins results in uncompensated magnetic moment, leading to a WFM behavior. The *M-H* curve at 150 K is a straight line (Inset of Fig. 10).

The ZFC data shows a typical AFM nature in the T_N region. The anomalies observed at 70 K appears to involve alignment of uncompensated-spins that leads to WFM. A similar situation of uncompensated-spin induced WFM was reported very recently in $Ca_3Mn_2O_7$ at ~ 110 K, below T_N (123 K) [31]. A key aspect for CMO is the correlation between the magnetic anomaly, the pronounced change in resistivity and a structural distortion. It has earlier been found that the evolution of WFM within the AFM-matrix in CMO leads to the observed MIT [25]. Hence it is clear that the distinct changes in magnetic susceptibility and in resistivity, are strongly connected to a structural distortion. This is evidence of a strong coupling between spin, charge and structure. A physical coexistence of FM and AFM magnetic situations may explain the observed magnetic glassiness [11, 24, 26, 32-34]. For CMO, the two successive transitions behave differently with respect to an applied DC field (clearly visible in Fig. 11). The suppression of the peak in $\chi(T)$ at 115 K by application of higher fields may suggest the existence of a spin-glass-like magnetic state.

The enhancement of the peak at 70 K with increasing fields cannot be explained within the framework of an ordinary spin glass-like state. Interestingly, none of the magnetic transitions shift in temperature with respect to frequency (Figs. 7a and 8a) and hence, they do not represent any typical spin-glass behavior. Thus, the results support that the existence of two magnetic transitions in CMO is not directly linked to a spin-glass situation [35, 36] and that the term magnetic-glass is more appropriate to describe the coexistence of magnetic phases.

Owing to the strong coupling due to the existence of MIT at the WFM-onset temperature, one may expect CMR behavior at low temperatures. Resistivity measurements were carried out under applied magnetic fields up to 9 T. The temperature dependence of the MR effect is shown in Fig. 12. The MR effect is defined as MR % = $\{[\rho(H) - \rho(0)]/\rho(0)\}\times 100$ [37], where $\rho(0)$ is the resistivity at zero field and $\rho(H)$ is the resistivity at the applied field H. The MR data in Fig. 12 show positive MR behavior (PMR) below T_{MIT} and negative behavior (NMR) above T_{MIT}. In CMO, metallic WFM domains are embedded in the insulating AFM-matrix, which is well-evidenced in R(T) and $\chi(T)$ dependences. On the low-temperature metallic side of the MIT, PMR behavior up to 550 % is observed at 4 K (Fig. 12a). On the insulator side of the MIT, NMR values of up to 3.5 % in magnitude is noticed at 112 K (Fig. 12b). The positive MR value decreases with increasing temperature, and switches into negative MR values near T_{MIT}, and persists further up to T_N.

In Fig. 13 we provide a simple model for explaining the uncommon variation in MR properties. In the metallic region $T < T_{MIT}$, the spin fluctuations induced by an applied magnetic field from the localized magnetism produce a PMR effect (Fig. 13a). For $T_N > T > T_{MIT}$, the suppression of spin disorder by the magnetic field leads to NMR (Fig. 13b).

The suggested coexistence of WFM and AFM as indicated by the DC and AC susceptibilities data can be interpreted in terms of a magnetically phase segregated state where the onset of glassiness leads to a marked increase in electrical resistivity. This situation may, as currently indicated, arise from structural distortions of the Mn sites below T_{MIT} that in turn affect exchange interactions and thereby alter the nature of the resistivity. This correlates with the observed crossover from a range with increasing resistivity with temperature (metal) to insulating behavior. As pointed by Battle *et al.* [15], for CMO there is a possibility of additional complexity arising from a very slight content of Mn^{3+} ions as a consequence of a minute oxygen non-stoichiometry stemming from the synthesis stage that indeed requires high pO_2 for achieving complete oxidation into Mn^{4+}. It is likely that such a Mn^{3+}/Mn^{4+} situation will occur for almost any CMO sample, but that the Mn^{3+} content can be tuned by post treatment (temperature, pO^2, holding time). The observation of simultaneous itinerant electron behavior (metal) and glassiness is governed by electron hopping via Mn-O-Mn bridges for the corner shared MnO_6-octahedra. The hopping is likely to be influenced by the structural distortion, which although being moderate in magnitude, definitely affects the Mn-O-Mn bond angles and orbital overlaps. .

We conclude that $Ca_4Mn_3O_{10}$ (CMO) undergoes a metal-insulator transition (MIT) at 70 K. The MIT is accompanied by a structural effect. Moreover, weak-ferromagnetic (WFM) behavior appears as a consequence of the slight structural distortion. The coincidence of the transition temperature with respect to changes in electrical and magnetic behavior, as well in the degree of orthorhombic distortion shows that these phenomena are bulk effects and not grain boundary effects. The emergence of WFM and MIT in the same temperature interval of an otherwise single-phase material indicates a strong coupling, which in turn gives rise to the observed MR effects in CMO. The switching of MR behavior from positive to negative at the MIT temperature is unique. Thus, CMO is a fascinating system for further theoretical and experimental exploration.

ACKNOWLEDGMENT

The authors acknowledge financial support from the Research Council of Norway via the FRINATEK project 221905, NOvel Features of Complex Oxides (NOFCO). The authors thank Dr. Susmit Kumar and M.Sc. Asbjørn S. Fjellvåg for their support. We gratefully acknowledge the staff at the Swiss-Norwegian Beam Lines (SNBL), ESRF, France, for technical support.

References

1. Y. Takura, Colossal Magnetoresistive Oxides, Gordon and Breach Science, Singapore, 2000.
2. R. M. Kusters, J. Singleton, D. A. Keen, R. Mcgreevy, W. Hayes, Physica B 155 (1989) 362.
3. R. V. Helmolt, J. Wecker, B. Holzapfel, L. Schultz, K. Samwer, Phys. Rev. Lett. 71 (1993) 2331.
4. R. C. Yu, S. Y. Li, J. L. Zhu, F. Y. Li, Z. Zhang, C. Q. Jin, I. G. Voigt-Martin, J. Phys.: Condens. Matter 14 (2002) 11119.
5. Y. Tokura, Y. Tomioka, H. Kuwahara, A. Asamitsu, Y. Moritomo, M. Kasai, J. Appl. Phys. 79 (1996) 5288.
6. T. Hotta, A. L. Malvezzi, E. Dagotto, Phys. Rev. B 62 (2000) 9432.
7. E. Dagotto, T. Hotta, A. Moreo, Phys. Rep. 344 (2001) 1.
8. E. Dagotto, Science 309 (2005) 257.
9. M. Fäth, S. Freisem, A. A. Menovsky, Y. Tomioka, J. Aarts, J. A. Mydosh, Science 285 (1999) 1540.
10. Y. Moritomo, A. Asamitsu, H. Kuwahama, Y. Tokura, Nature 380 (1996) 141.
11. S. H. Chun, Y. Lyanda-Geller, M. B. Salamon, R. Suryanarayanan, G. Dhalenne, A. Revcolevschi, J. Appl. Phys. 90 (2001) 6307.
12. R. C. Yu, S. Y. Li, J. L. Zhu, F. Y. Li, Z. Zhang, C. Q. Jin, I. G. Voigt-Martin, J. Appl. Phys. 90 (2001) 6302.
13. J. Lago, P. D. Battle, M. J. Rosseinsky, A. I. Coldea, J. Singleton, J. Phys.: Condens. Matter 15 (2003) 6817.
14. J. B. MacChesney, H. J. Williams, J. F. Potter, R. C. Sherwood, Phys. Rev. 164 (1967) 779.
15. P. D. Battle, M. A. Green, J. Lago, J. E. Millburn, M. J. Rosseinsky, J. F. Vente, Chem. Mater. 10 (1998) 658.
16. J. Lago, P. D. Battle, M. J. Rosseinsky, J. Phys.: Condens. Matter 12 (2000) 2505.
17. H. J. Rossel, P. Goodman, S. Bulcock, R. H. March, S. J. Kennedy, T. J. White, F. J. Lincoln, S. Murray, Aust. J. Chem. 49 (1996) 205.
18. A. I. Mihut, L. E. Spring, R. I. Bewley, J. Phys.: Condens. Matter 10 (1998) L717.
19. P. Manimuthu, A. O. Sjåstad, H. Fjellvåg, IEEE Trans. Mag. 53 (2017) 11.
20. M. U. Nagell, W. A. Sławińskia, P. Vajeeston, H. Fjellvåg, A. O. Sjåstad, Solid State Ionics 305 (2017) 7.
21. V. Dyadkin, P. Pattison, V. Dmitriev, D. Chernyshov, J. Synchrotron Rad. 23 (2016) 825.
22. Bruker-AXS TOPAS V5: General profile and structure analysis software for powder diffraction data, Bruker AXS, Karlsruhe, Germany, 2013.
23. N. F. Mott, Rev. Mod. Phys. 40 (1968) 667.
24. M. Imada, A. Fujimori, Y. Tokura, Rev. Mod. Phys. 70 (1998) 1039.
25. P. D. Battle, M. A. Green, N. S. Laskey, J. E. Millburn, M. J. Rosseinsky, S. P. Sullivan, J. F. Vente, Chem. Commun. 6 (1996) 767.
26. M. Tokumoto, Y. Nishihara, K. Oka, H. Unoki, Nature 330 (1987) 48.

27. M. Balanda, Acta Phys. Pol. A 124 (2013) 964.
28. S. Kundu, T. K. Nath, J. Magn. Magn. Mater. 322 (2010) 2408.
29. A. K. Pramanik, A. Banerjee, J. Phys.: Condens. Matter 20 (2008) 275207.
30. A. Bajpai, A. Banerjee, Phys. Rev. B 55 (1997) 12439.
31. P. Sahlot, A. M. Awasthi, J. Mag. Mag. Mater. 493 (2020) 165732.
32. P. Ravindran, R. Vidya, P. Vajeeston, A. Kjekshus, H. Fjellvåg, B. C. Hauback, Solid State Commun. 124 (2002) 293.
33. S. B. Roy, M. K. Chattopadhyay, M. A. Manekar, K. J. S. Sokhey, P. Chaddah, Bull. Mater. Sci. 29 (2006) 623.
34. X. L. Qian, D. M. Deng, Y. Jin, B. Lu, S. X. Cao, J. C. Zhang, J. Appl. Phys. 115 (2014) 193902.
35. M. K. Chattopadhyay, M. A. Manekar, A. O. Pecharsky, V. K. Pecharsky, K. A. Gschneidner, J. Moore, G. K. Perkins, Y. V. Bugoslavsky, S. B. Roy, P. Chaddah, L. F. Cohen, Phys. Rev. B 70 (2004) 214421.
36. M. K. Chattopadhyay, S. B. Roy, P. Chaddah, Phys. Rev. B 72 (2005) 180401.
37. X. X. Zhang, J. M. Hernandez, Europhys. Lett. 47 (1999) 487.
38. H. Li, Y. Xiao, B. Schmitz, J. Persson, W. Schmidt, P. Meuffels, G. Roth, T. Brückel, Scientific Reports 2 (2012) 750.

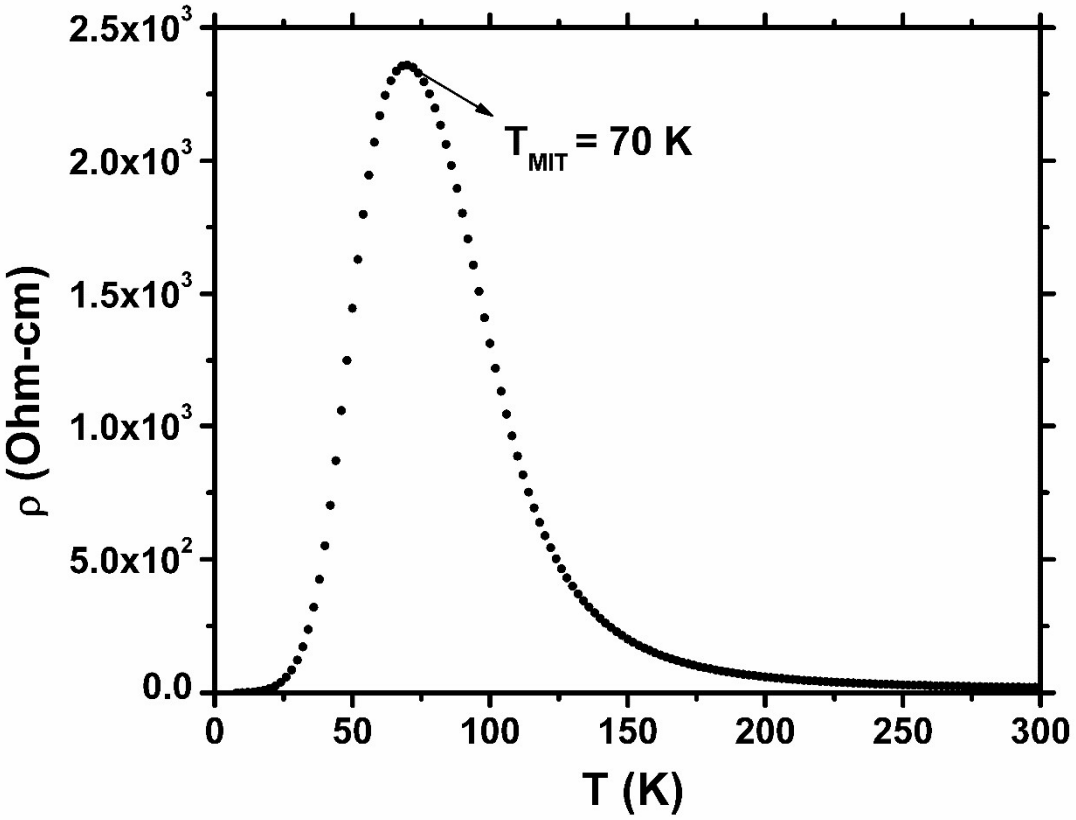

Fig. 1. Variation of resistivity as a function of temperature showing the metal-to-insulator transition at 70 K.

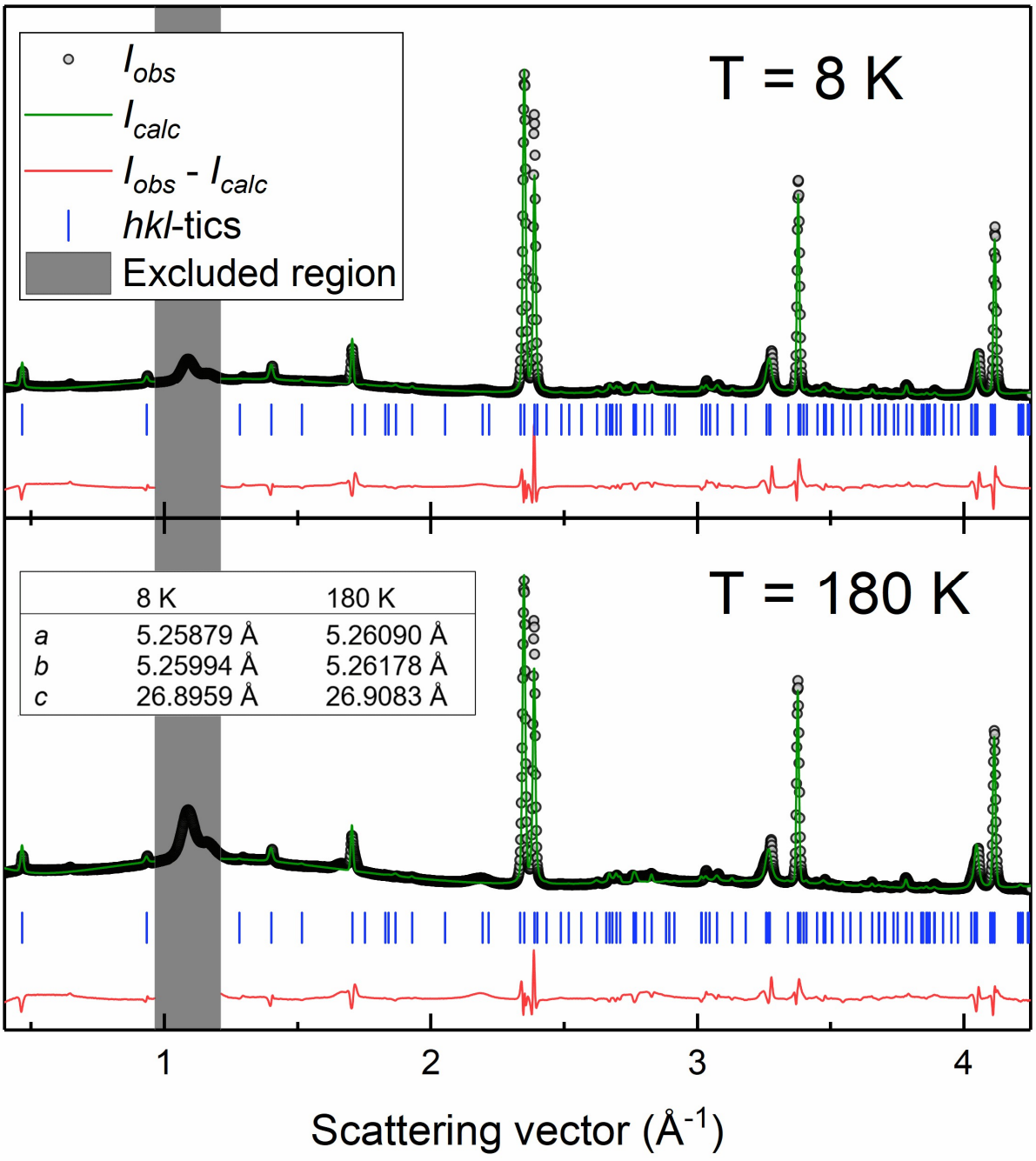

Fig. 2. Rietveld refinements of synchrotron XRD patterns of $Ca_4Mn_3O_{10}$ in space group *Pbca* at two different temperatures (below and above MIT), showing a single-phase sample. The shaded region around ~1 Å^{-1} corresponds to the diffraction signal from the sample environment (vacuum grease from capillary mounting).

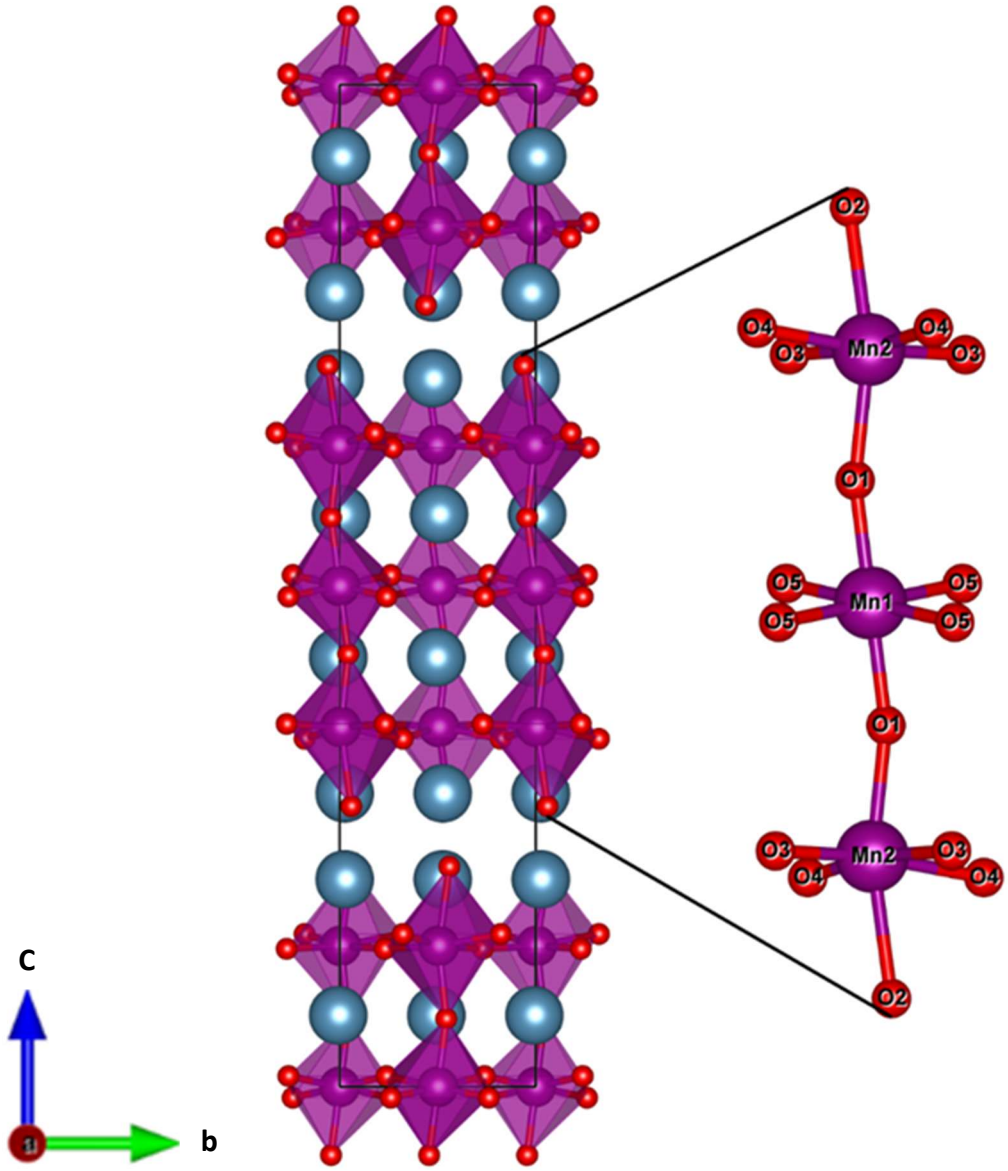

Fig. 3. Crystal structure of $Ca_4Mn_3O_{10}$ at 8 K; space group *Pbca*. Blue atoms correspond to calcium, purple to manganese and red to oxygen.

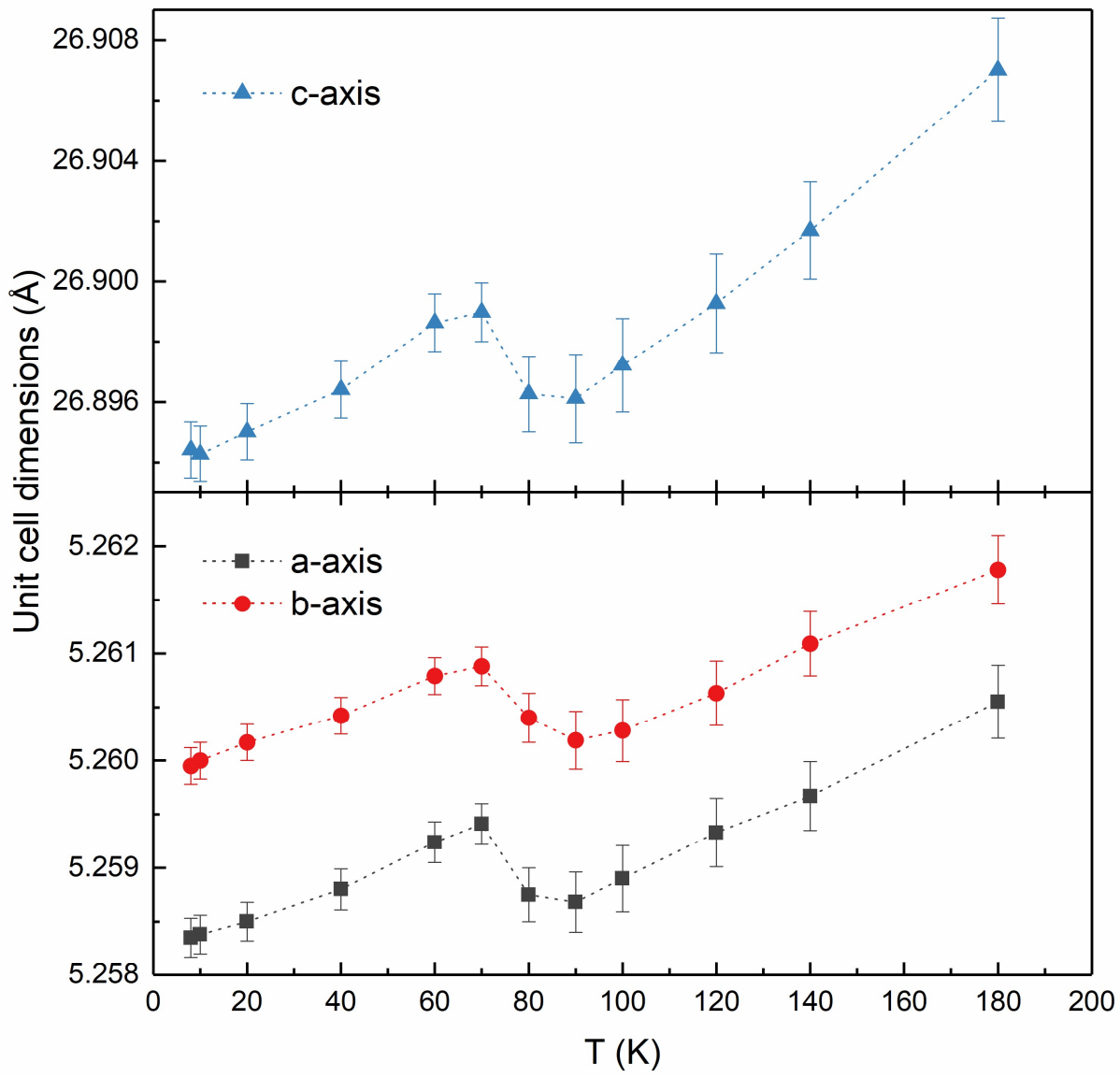

Fig. 4. Temperature dependence of unit cell dimensions (a, b, and c) derived from Rietveld analysis of synchrotron powder XRD data, showing an anomaly at 70 K.

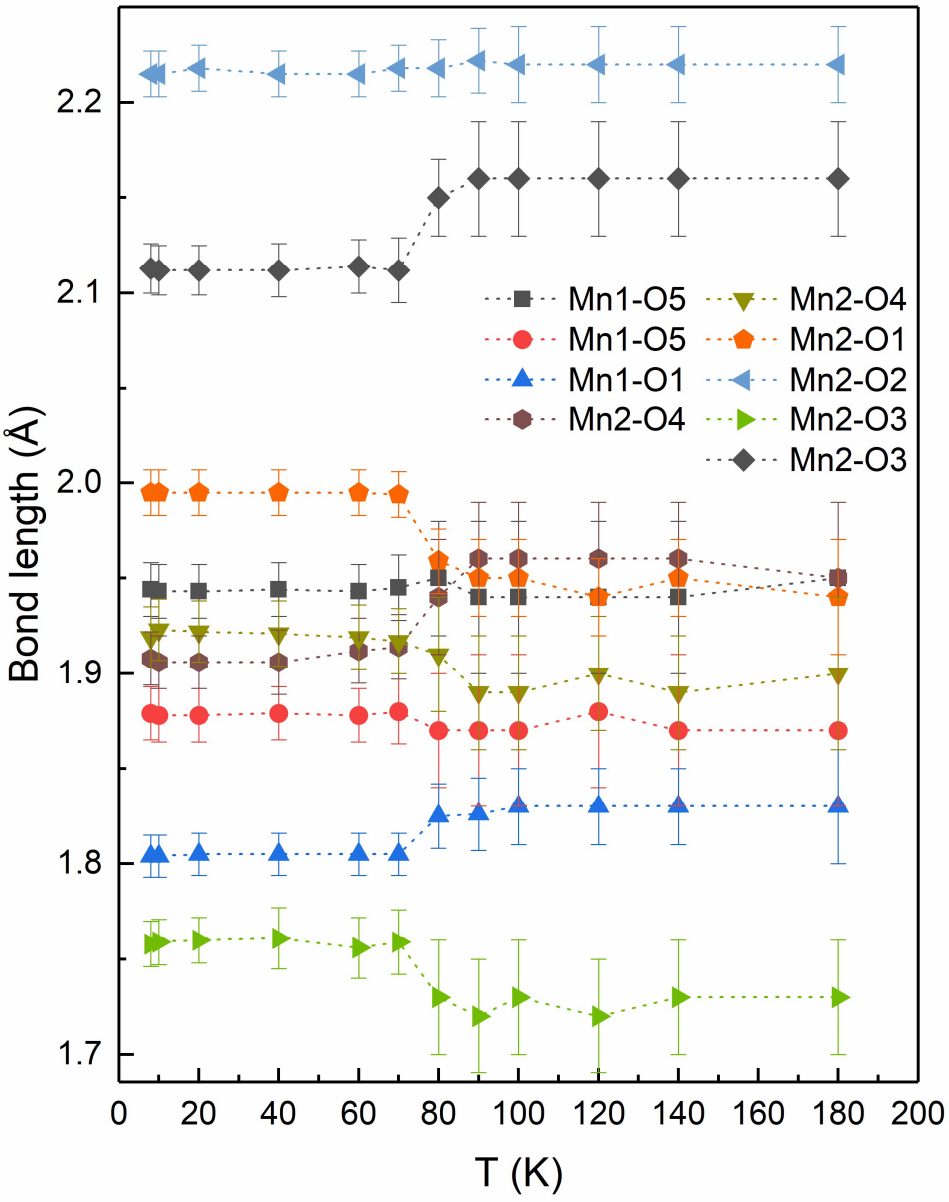

Fig. 5. Variation of Mn-O bond lengths between 10 and 180 K. Equivalent distances are not show.

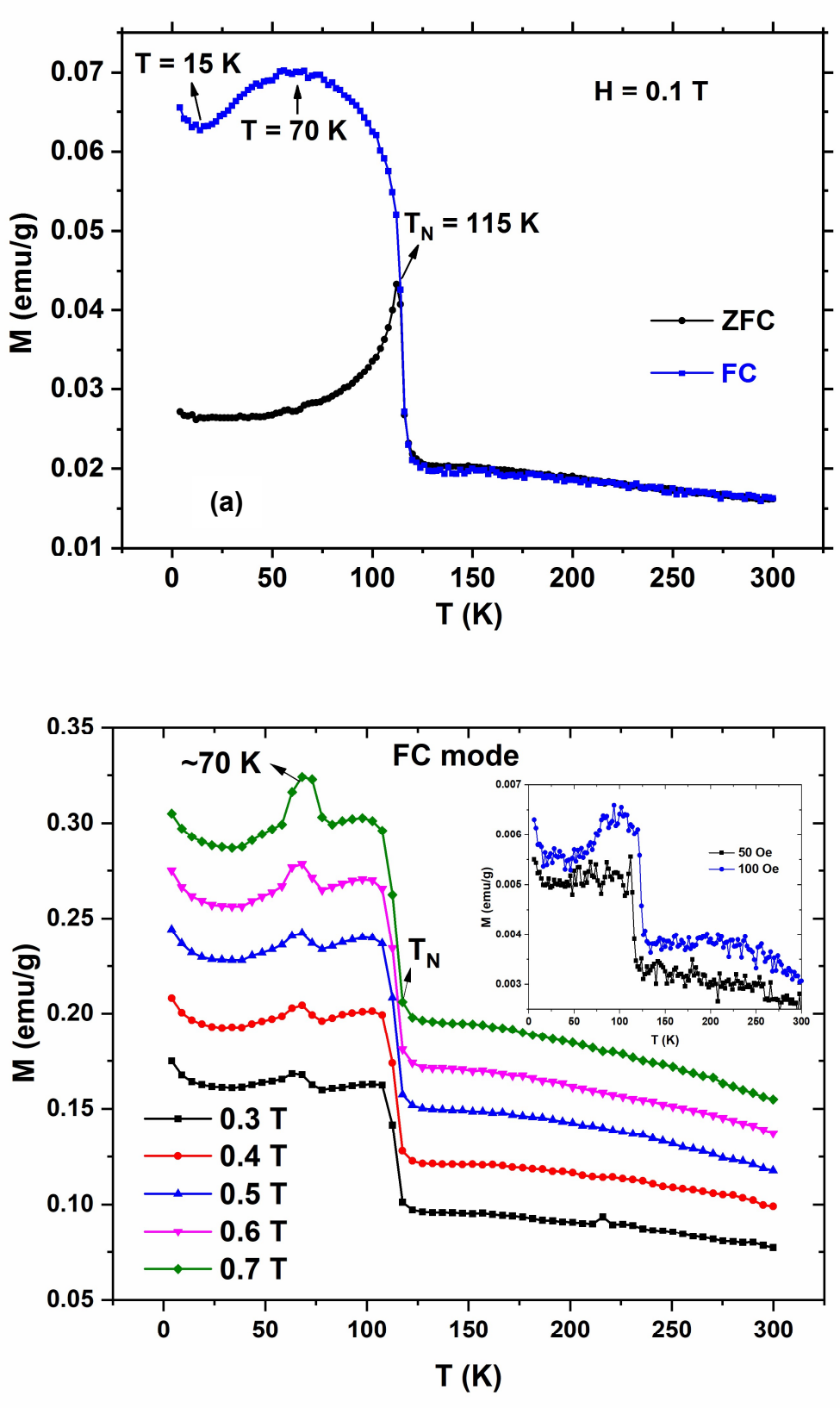

Fig. 6. Temperature dependence of χ_{dc} susceptibility measured in a field of (a) H = 0.1 T at FC and ZFC conditions; (b) H = 0.3 – 0.7 T for FC conditions; and inset (b) H = 50 – 100 Oe for FC conditions.

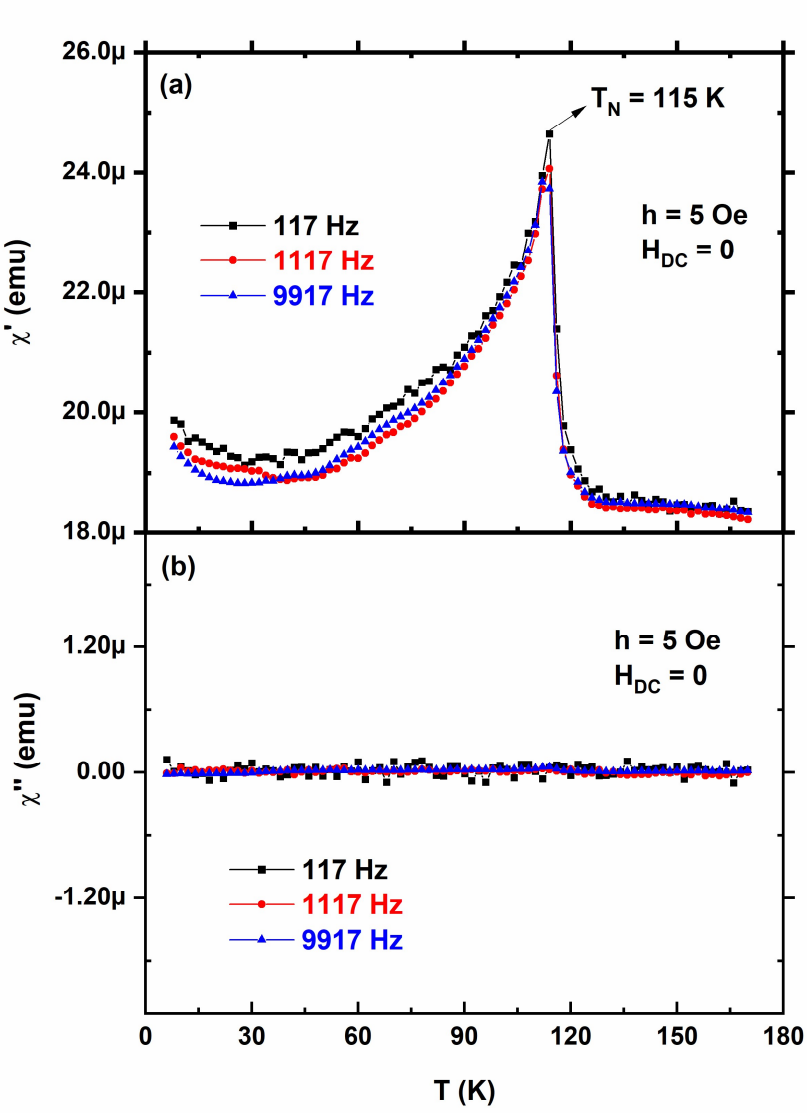

Fig. 7. Temperature variation of the real (a) and imaginary (b) part of the χ_{ac} magnetic susceptibility at different frequencies in a probing AC drive field (h) of 5 Oe (no DC field, H_{DC} = 0).

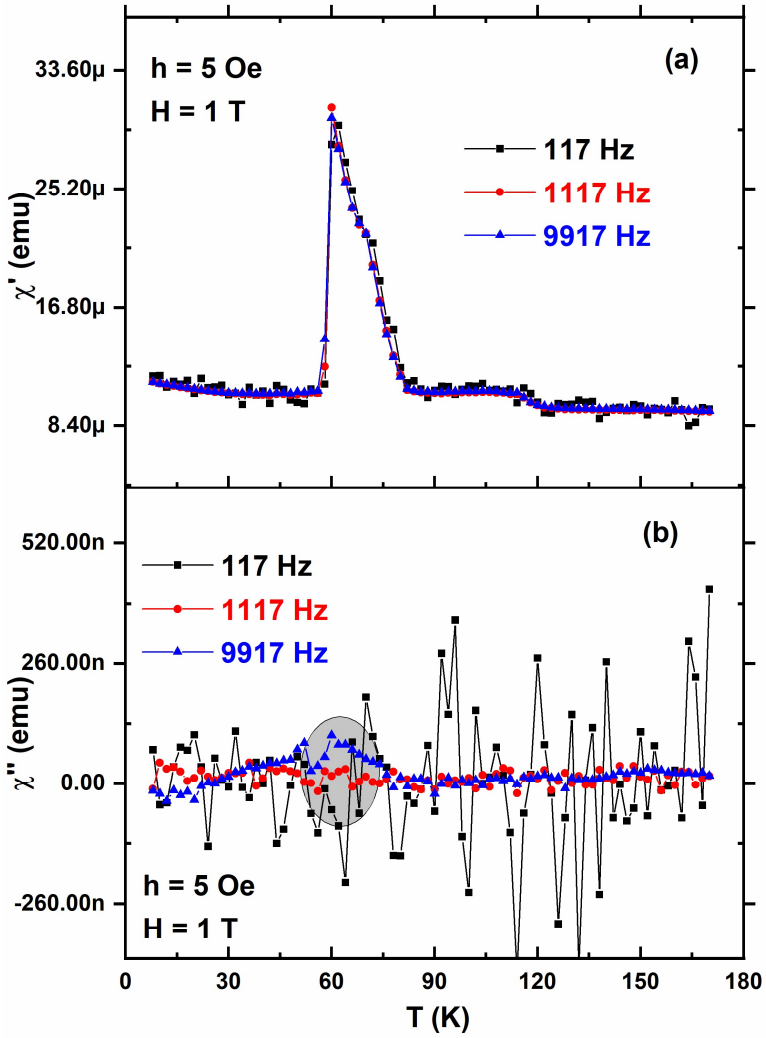

Fig. 8. Temperature variation of real (a) and imaginary (b) part of the χ_{ac} magnetic susceptibility at 117, 1117 and 9917 Hz for a drive field of 5 Oe and with an external DC field of 1 T.

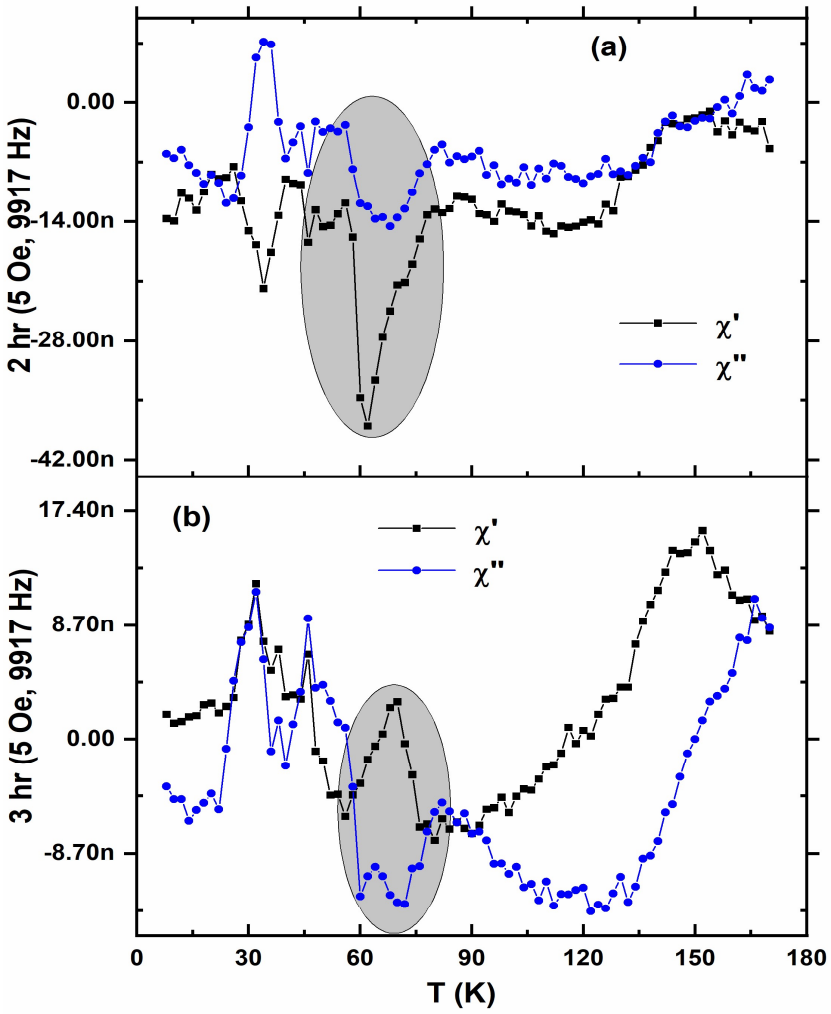

Fig. 9. Temperature variation of (a) second-order (2 hr) and (b) third-order (3 hr) non-linear χ_{ac} susceptibilities at 9917 Hz in an applied DC field of 1 T.

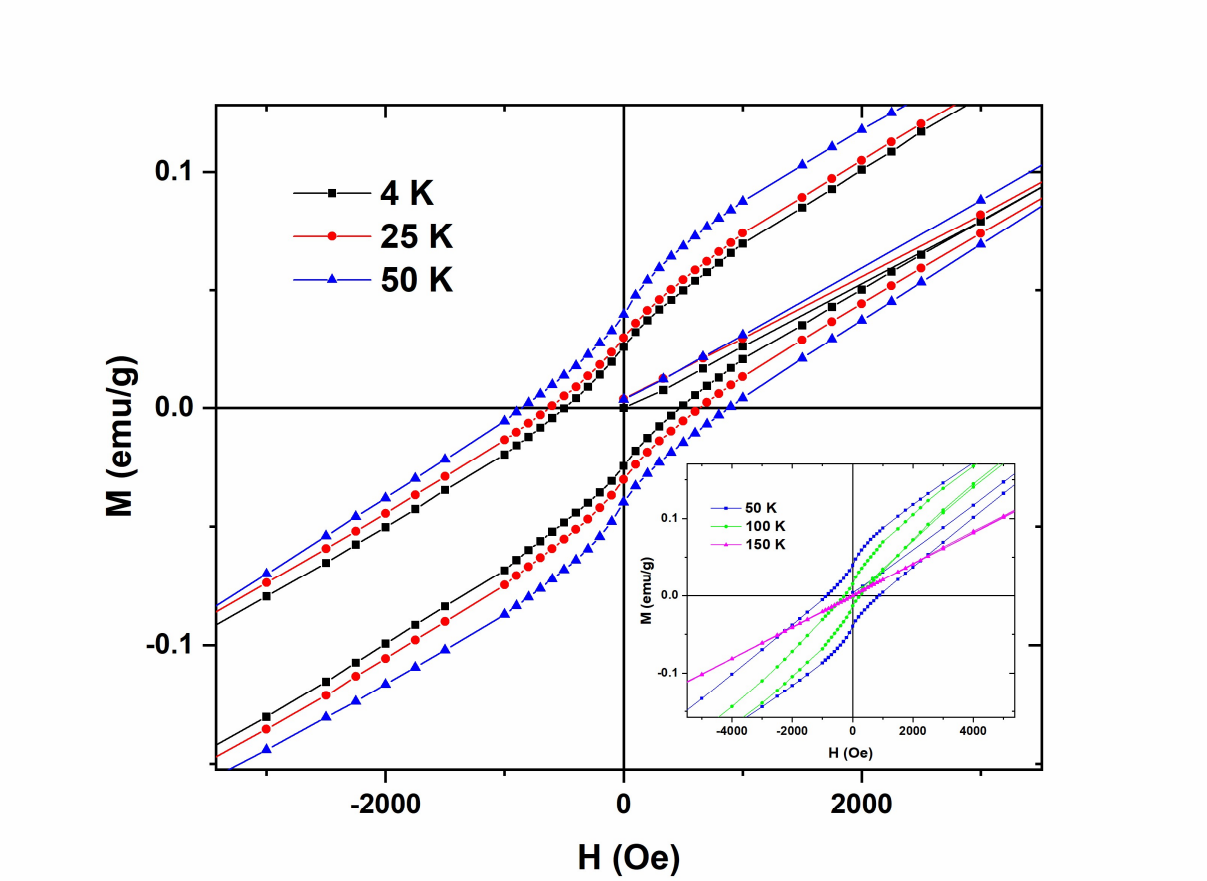

Fig. 10. *M-H* loops of $Ca_4Mn_3O_{10}$ at various temperatures (4, 25 and 50 K) for applied magnetic field range (-9 kOe ≤ +9 kOe). Actual measurements were done for the applied magnetic field in the range from -9 kOe to +9 kOe but here shown zoomed *M-H* loops for the clear view. Inset: *M-H* loops measured at 50, 100 and 150 K.

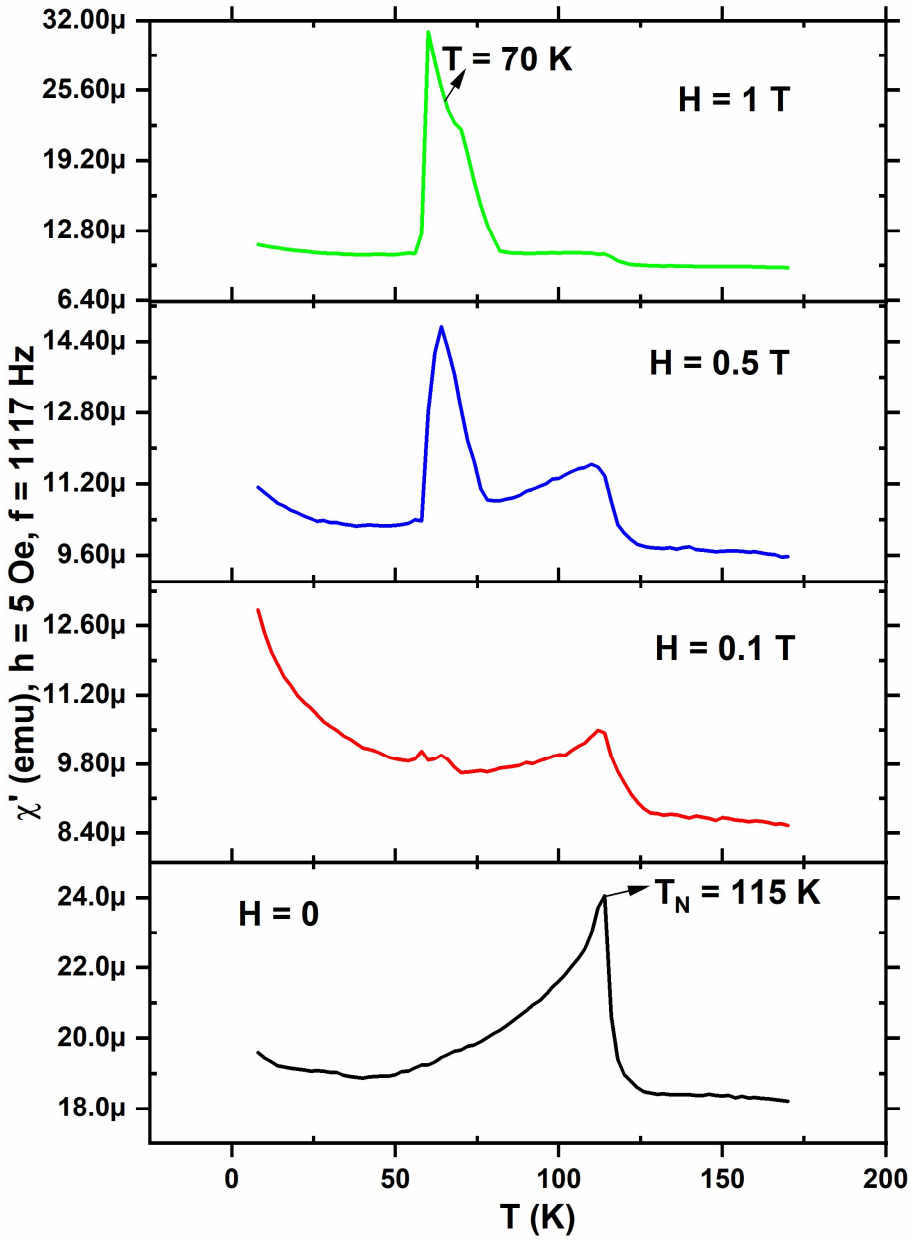

Fig. 11. Temperature variation of the real part of χ_{ac} magnetic susceptibility under different DC magnetic fields at 1117 Hz.

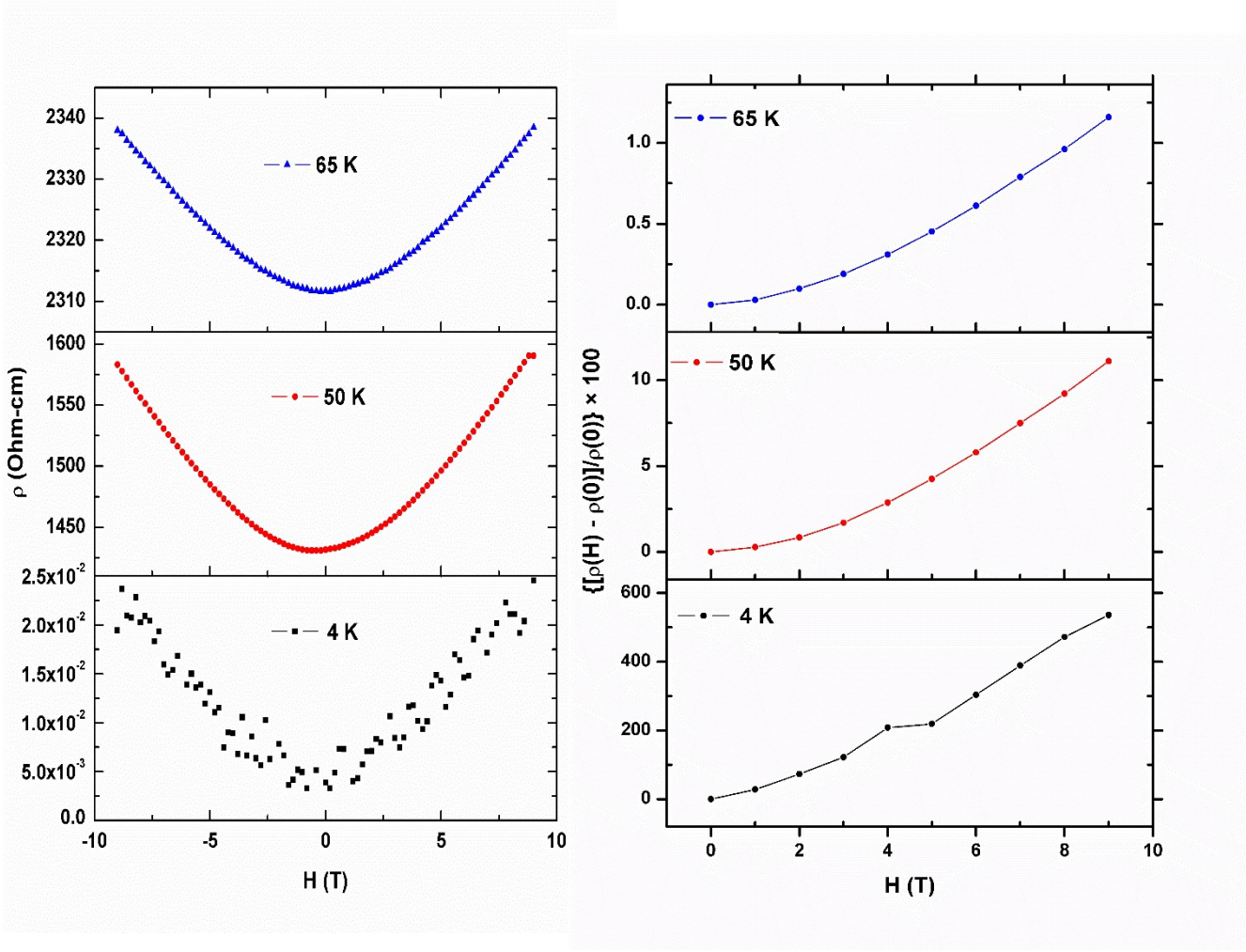

Fig. 12a. Left: Resistivity as a function of the applied magnetic field at T < 70 K. Right: Positive MR at 4, 50 and 65 K.

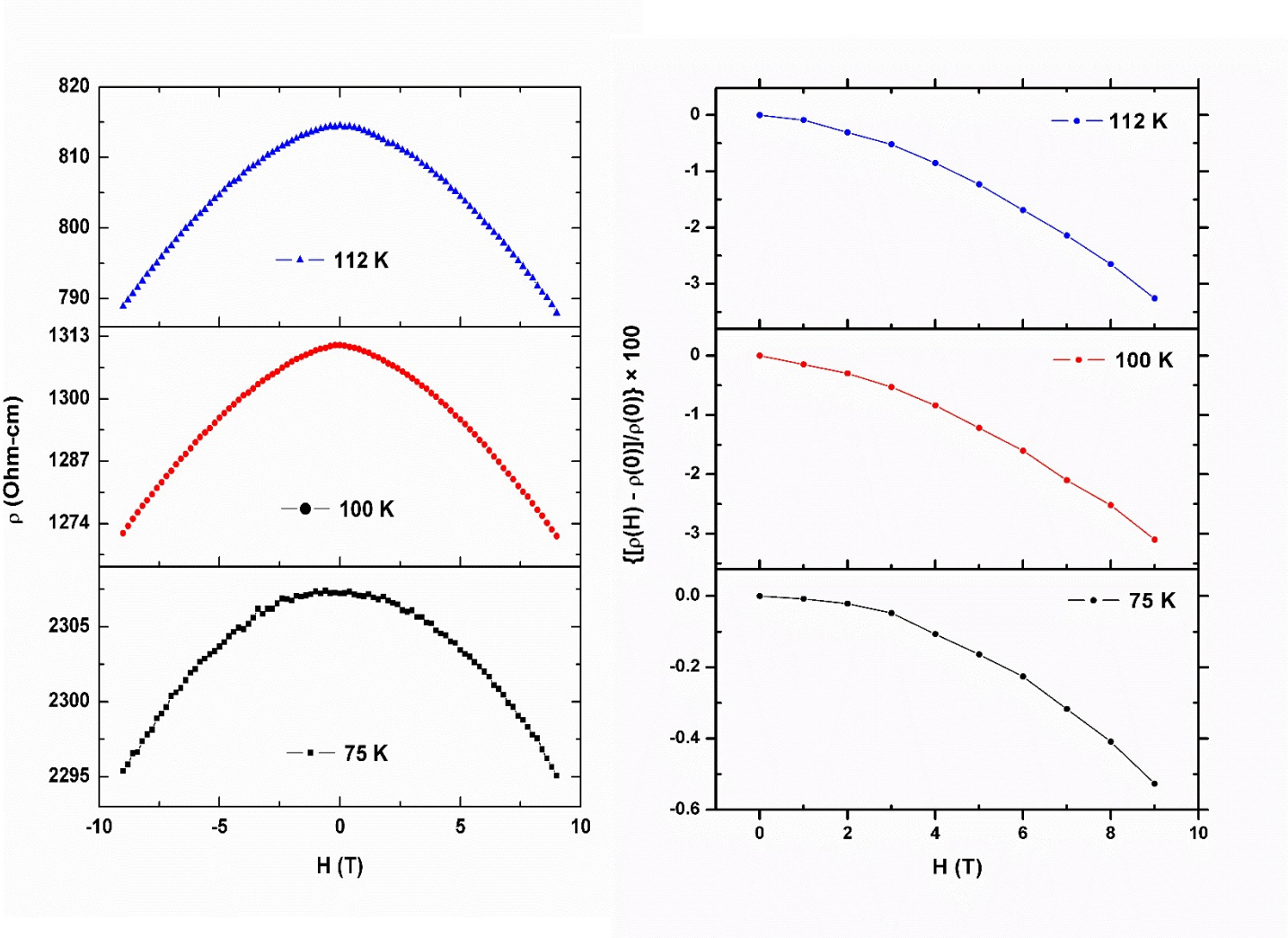

Fig. 12b. Left: Resistivity as a function of the applied magnetic field at T > 70 K. Right: Negative MR at 75, 100 and 112 K.

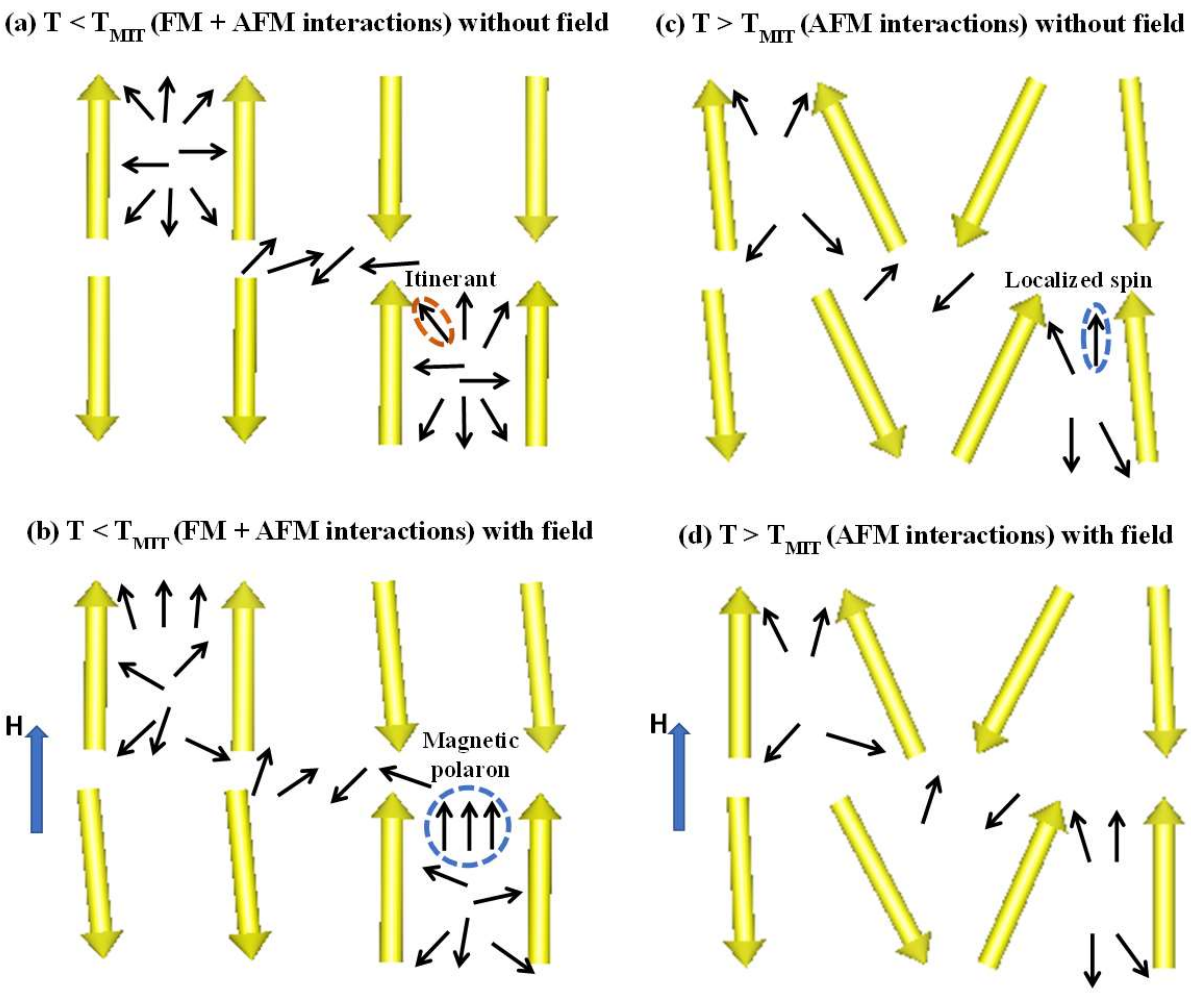

Fig. 13. Schematic illustration of the spin states with and without applied magnetic field. Yellow arrows: spin moment, Black arrows, interaction between the spin moments; Red dotted circle, itinerant spin; Blue dotted circle, localized spin. (a, b) T < 70 K, coexistence of WFM and AFM interactions with itinerant moments. The applied magnetic field localizes the itinerant moments resulting in the formation of magnetic polarons and the consequent positive MR. (c, d) $T_N > T > 70$ K, only AFM spins with localized moments. The applied magnetic field aligns the AFM spins, leading to a decrease of the electron-spin scattering and resultant the negative MR.

SUPPLEMENTARY INFORMATION

Table S1: List of refined parameters. The table indicates which parameters were refined for individual datasets, datasets measured at the same distance, datasets measured at the same temperature and all datasets simultaneously.

	Individual	Distance	Temperature	All
Lattice parameters			×	
Atomic position			×	
Zero point error	×			
Absorption				×
Background	×			
Peak shape		×		

Table S2: Characteristic features of the SR–XRD datasets and list of refined parameters.

Data points	3358 at each distance
Range for different detector distances	100mm: 0 – 44.28° 200mm: 0 – 34.68° 300mm: 0 – 28.20° 400mm: 0 – 23.63° 500mm: 0 – 20.22°
Excluded regions	6.4 – 7.9°
Wavelength (Å)	0.71490
Scale factor	5
Zero point error	5
Absorption correction	1[a]
Profile parameters	2×5[b] + 7
Unit cell dimensions	3
Atomic positions	24
Atomic displacement parameters	1[a]
Background coefficients	5
Refined parameters	61

[a] Same for all scans

[b] Same for all distances

Table S3: Crystallographic information for $Ca_4Mn_3O_{10}$ in space group *Pbca*, [*a* = 5.25835(18) Å, *b* = 5.25995(17) Å, *c* = 26.8944(9) Å] from SR-XRD at 8 K.

Atom	Wycoff	*x*	*y*	*z*	U_{iso}
Ca1	8c	0.4866(17)	0.4905(10)	0.07037(15)	0.014944(7)
Ca2	8c	0.006(2)	0.0242(13)	0.20823(12)	0.014944(7)
Mn1	4b	0	0.5	0	0.014944(7)
Mn2	8c	0.4895(12)	0.0044(10)	0.14010(10)	0.014944(7)
O1	8c	0.489(4)	0.048(2)	0.0664(4)	0.014944(7)
O2	8c	0.515(5)	0.056(3)	0.2217(4)	0.014944(7)
O3	8c	0.824(2)	0.227(2)	0.1391(5)	0.014944(7)
O4	8c	0.180(2)	0.823(3)	0.1506(5)	0.014944(7)
O5	8c	0.266(2)	0.257(3)	-0.0161(5)	0.014944(7)

Table S4: Unit cell dimensions of $Ca_4Mn_3O_{10}$ from Rietveld refinements at temperatures between 8 and 180 K.

Temperature (K)	*a* (Å)	*b* (Å)	*c* (Å)	U_{iso}
8	5.25835	5.25995	26.89442	0.014944
10	5.25838	5.26	26.89428	0.01497
20	5.2585	5.26017	26.89502	0.014972
40	5.2588	5.26042	26.89641	0.015006
60	5.25924	5.26079	26.89863	0.014942
70	5.25941	5.26088	26.89898	0.014909
80	5.25875	5.2604	26.89627	0.013564
90	5.25868	5.26019	26.89612	0.013508
100	5.2589	5.26028	26.89722	0.013621
120	5.25933	5.26063	26.89927	0.013537
140	5.25967	5.26109	26.90169	0.01373
180	5.26055	5.26178	26.90701	0.01417

Table S5: Atomic positions (only x-coordinates) of $Ca_4Mn_3O_{10}$ from Rietveld refinements for measured temperatures

Temperature (K)	x_Ca1	x_Ca2	x_Mn1	x_Mn2	x_O1	x_O2	x_O3	x_O4	x_O5
8	0.48664	0.00554	0	0.48954	0.48896	0.51483	0.82369	0.18001	0.26627
10	0.48675	0.00555	0	0.4896	0.48884	0.51513	0.8238	0.18002	0.26624
20	0.48663	0.00553	0	0.48961	0.48904	0.51477	0.82382	0.17983	0.26605
40	0.4868	0.00556	0	0.48952	0.48842	0.51531	0.82375	0.18031	0.26705
60	0.48691	0.00594	0	0.48959	0.48864	0.51538	0.82414	0.17941	0.26574
70	0.48729	0.00611	0	0.48971	0.48796	0.51659	0.82388	0.1793	0.26671
80	0.48867	0.01015	0	0.48921	0.48119	0.52781	0.82977	0.17471	0.26677
90	0.48909	0.01101	0	0.48888	0.47761	0.5334	0.83219	0.17248	0.26561
100	0.48899	0.01129	0	0.48905	0.47754	0.53372	0.83287	0.1715	0.26329
120	0.48926	0.01134	0	0.48906	0.47593	0.53411	0.83299	0.17196	0.26436
140	0.48929	0.0114	0	0.48891	0.47632	0.53406	0.83228	0.17232	0.26492
180	0.48949	0.01193	0	0.48855	0.47298	0.53546	0.83267	0.17359	0.26568

Table S6: Atomic positions (only y-coordinates) of $Ca_4Mn_3O_{10}$ from Rietveld refinements for measured temperatures

Temperature (K)	y_Ca1	y_Ca2	y_Mn1	y_Mn2	y_O1	y_O2	y_O3	y_O4	y_O5
8	0.49048	0.02423	0.5	0.00441	0.04834	0.0564	0.22735	0.82343	0.25745
10	0.49052	0.02438	0.5	0.00457	0.04842	0.05617	0.22739	0.82358	0.25736
20	0.49071	0.02444	0.5	0.00481	0.04832	0.0564	0.22736	0.82372	0.25712
40	0.49075	0.02464	0.5	0.00492	0.04809	0.05578	0.22741	0.82373	0.25806
60	0.49096	0.02436	0.5	0.00495	0.04788	0.05515	0.22763	0.82436	0.25698
70	0.4915	0.02492	0.5	0.00564	0.04767	0.05384	0.22801	0.82424	0.25808
80	0.49531	0.0241	0.5	0.00678	0.05129	0.03803	0.23317	0.8245	0.25601
90	0.49951	0.02318	0.5	0.00749	0.05125	0.01306	0.23267	0.82229	0.25574
100	0.5001	0.02232	0.5	0.00758	0.05115	0.00898	0.23228	0.82275	0.25334
120	0.50037	0.02295	0.5	0.00746	0.04899	0.00775	0.23194	0.8229	0.25455
140	0.49977	0.0232	0.5	0.00769	0.04927	0.01345	0.23234	0.82305	0.25482
180	0.50119	0.02349	0.5	0.00709	0.04651	0.00699	0.23063	0.82284	0.25606

Table S7: Atomic positions (only z-coordinates) of $Ca_4Mn_3O_{10}$ from Rietveld refinements for measured temperatures

Temperature (K)	z_Ca1	z_Ca2	z_Mn1	z_Mn2	z_O1	z_O2	z_O3	z_O4	z_O5
8	0.07037	0.20823	0	0.1401	0.0664	0.22169	0.13913	0.15058	-0.01608
10	0.07037	0.20824	0	0.14011	0.06642	0.2217	0.13914	0.1506	-0.01604
20	0.07036	0.20823	0	0.1401	0.06644	0.22175	0.13913	0.15059	-0.01602
40	0.07035	0.20824	0	0.1401	0.0664	0.22174	0.1391	0.15059	-0.01608
60	0.07034	0.20823	0	0.14008	0.06641	0.22173	0.13921	0.15059	-0.01599
70	0.07032	0.20826	0	0.14005	0.06639	0.22179	0.13926	0.15058	-0.01616
80	0.07024	0.20836	0	0.13932	0.06696	0.22119	0.139	0.15177	-0.01533
90	0.07017	0.20851	0	0.13906	0.06701	0.22117	0.1393	0.15194	-0.01544
100	0.07016	0.20854	0	0.13895	0.06706	0.22104	0.1395	0.15198	-0.01541
120	0.07013	0.2086	0	0.13884	0.06706	0.22097	0.13959	0.15186	-0.01557
140	0.0701	0.20857	0	0.13891	0.06697	0.22098	0.13961	0.15166	-0.0156
180	0.07004	0.2086	0	0.13879	0.06704	0.22076	0.13962	0.15154	-0.01566